Energy materials

Novel synthesis and electrochemical investigations of ZnO/C composites for lithium-ion batteries

E. Thauer[1],*, G. S. Zakharova[2,3], E. I. Andreikov[4], V. Adam[1], S. A. Wegener[1],
J. -H. Nölke[1], L. Singer[1], A. Ottmann[1], A. Asyuda[5], M. Zharnikov[5], D. M. Kiselkov[6],
Q. Zhu[7], I. S. Puzyrev[4], N. V. Podval'naya[2], and R. Klingeler[1,8]

[1] Kirchhoff Institute of Physics, Heidelberg University, Heidelberg, Germany

[2] Institute of Solid State Chemistry, Ural Division, Russian Academy of Sciences, Yekaterinburg, Russia

[3] Ural Federal University, Yekaterinburg, Russia

[4] I.Ya. Postovskii Institute of Organic Synthesis, Ural Division, Russian Academy of Sciences, Yekaterinburg, Russia

[5] Applied Physical Chemistry, Heidelberg University, Heidelberg, Germany

[6] Institute of Technical Chemistry, Ural Division, Russian Academy of Sciences, Perm, Russia

[7] School of Material Science and Engineering, Wuhan University of Technology, Wuhan, China

[8] Centre for Advanced Materials, Heidelberg University, Heidelberg, Germany

ABSTRACT

For the first time, ZnO/C composites were synthesized using zinc glycerolate as a precursor through one-step calcination under a nitrogen atmosphere. The effect of the heat treatment conditions on the structure, composition, morphology as well as on the electrochemical properties regarding application in lithium-ion batteries are investigated. The products obtained by calcination of the precursor in nitrogen at 400—800 °C consist of zinc oxide nanoparticles and amorphous carbon that is *in-situ* generated from organic components of the glycerolate precursor. When used as anode material for lithium-ion batteries, the as-prepared ZnO/C composite synthesized at a calcination temperature of 700 °C delivers initial discharge and charge capacities of 1061 and 671 mAh g^{-1} at a current rate of 100 mA g^{-1} and hence 1.5 times more than bare ZnO, which reaches only 749/439 mAh g^{-1}. The native carbon improves the conductivity, allowing efficient electronic conductivity and Li-ion diffusion. By means of *ex-situ* XRD studies a two-step storage mechanism is proven.

🖄 Springer

Introduction

ZnO has attracted attention of a large community of researchers as an electrode material for lithium-ion batteries (LIBs) due to its low cost, environmental friendliness and high theoretical capacity in particular [1–4]. Assuming a two-step reaction mechanism that involves a conversion Eq. (1) and alloying process Eq. (2), as proposed by previous studies [5–7], up to 3 Li$^+$/f.u. can be reversibly stored corresponding to a theoretical capacity of 978 mAh/g:

$$ZnO + 2Li^+ + 2e^- \leftrightarrow Zn + Li_2O, \tag{1}$$

$$Zn + Li^+ + e^- \leftrightarrow LiZn. \tag{2}$$
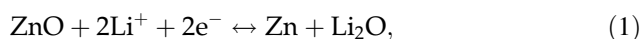
However, there are some challenges to overcome. One issue is the large volume change of ZnO during the dis-/charge process resulting in pulverization of the electrode material [8]. Furthermore, the studies of Pelliccione et al. [6] and Park et al. [9] revealed the limited reversibility of the conversion reaction Eq. (1), which depends on the size of the electrochemically formed zinc particles, as additional reason behind the rapid capacity fading. Li$_2$O can only be partially decomposed due to its poor reactivity and low lithium ion conductivity [10]. Another factor that limits the practical application of ZnO for electrochemical energy storage is its poor electrical conductivity [11]. To overcome these difficulties and to enhance the electrochemical performance of ZnO-based anodes, hybridizing ZnO with varieties of conductive carbon materials is frequently employed. Carbonaceous materials can prevent the aggregation of ZnO nanoparticles and maintain the structural stability of the anode during charge/discharge processes. ZnO nanoparticles anchored on the surface of carbon nanotubes (CNT) have been shown to deliver a reversible capacity of 602 mAh g^{-1} at 100 mA g^{-1} for up to 50 cycles, i.e., superior cycling and rate performances [12]. Similarly, a ZnO/graphene anode exhibits an initial specific capacity of 850 mAh g^{-1} at 0.1 C and good cycling stability (capacity decay ∼8% after 50 cycles) [13]. Also, films of ZnO nanosheets coated with 350 Å thick graphite layers showed specific capacity values of ∼ 600 mAh g^{-1} at 1 A g^{-1} after 100 cycles [14].

Various synthesis methods and approaches have been used in the literature to fabricate ZnO/C composites. Yang et al. [15] reported the synthesis of porous carbon coated ZnO quantum dots by the carbonization of metal–organic frameworks. As-obtained composites exhibit a reversible capacity of 919 mAh g^{-1} over 100 cycles at 100 mA g^{-1}. The porous ZnO/C microboxes prepared by annealing of the analogous metal–organic framework carboxylate groups deliver an initial discharge capacity of 1290 mAh g^{-1} and reach a high reversible capacity of 716 mAh g^{-1} after 100 cycles at a current density of 100 mA g^{-1} [16]. Bai et al. [17] have synthesized ZnO/C nanospheres by a one-step co-pyrolysis method using Zn powder and acetylacetone as starting materials. As-prepared ZnO/C nanospheres show a reversible capacity of 440 mAh g^{-1} at a current density of 100 mA g^{-1} after 50 cycles. Electrospinning and subsequent thermal treatment by Zhao et al. yielded a ZnO/carbon nanofiber composite, which delivers a reversible capacity of 702 mAh g^{-1} at a current density of 200 mA g^{-1} [18]. Hydrothermally fabricated core–shell ZnO/C nanospheres by Liu et al. [19] obtained from Zn-resorcinol–formaldehyde polymer followed by carbonization at 650 °C under inert atmosphere show a capacity of 496 mAh g^{-1} after 200 cycles at a current density of 82.5 mA g^{-1}. Microwave-assisted solvothermal synthesis permitting to reduce the time of reaction was performed to produce ZnO/C composites using sucrose as carbon source [20]. However, these methods always need multi-step or strict experimental conditions which increase the costs and limit large-scale production.

There are, however, one-step methods as well, with calcination under a nitrogen atmosphere for the synthesis of ZnO/C composites being probably the most efficient, easily implementable, and low-cost approach. In this case, organometallic complexes suggested for thermal treatment such as zinc citrate dihydrate $(C_6H_5O_7)_2Zn_3 \cdot 2H_2O$ [21–24] and zinc tartrate $C_4H_4ZnO_6$ [25] can serve as precursors for both, ZnO and carbon.

Summarizing, although a significant progress has already been achieved, developing a facile route to synthesize carbon coated nanosized materials remains an important task to further improve the performance of ZnO-based anode materials. In the present paper, based on the results of our previous work [26], a synthetic route involving a thermal treatment of organometallic compounds was developed to prepare carbon-composited metal oxide. The formation of ZnO/C composites has been

successfully realized by heat treatment of zinc glycerolate (ZnGly) under inert atmosphere. The organic component of ZnGly partially transformed into carbon resulting in the formation of ZnO/C composites. Additionally, potential applications of the ZnO/C composites as anode materials for lithium-ion batteries were investigated.

Experimental

Materials preparation

Zinc acetate dihydrate $(CH_3COO)_2Zn \cdot 2H_2O$ and freshly distilled glycerol (analytical grade) were used as the starting materials for the synthesis of zinc glycerolate $ZnC_3H_6O_3$. The ZnGly precursor was prepared via a polyol-mediated synthesis based on Dong's work [27]. Typically, 2.0 g $(CH_3COO)_2$-$Zn \cdot 2H_2O$ and 1 ml of distilled water were added to 50 mL of glycerol in a 100-mL round-bottom flask. This solution was heated to 160 °C and refluxed under Ar flow for 1 h. After cooling to room temperature, the resulting colorless precipitate, zinc glycerolate, was collected using centrifugation, washed with ethanol, and dried at 80 °C for 60 min. Finally, ZnO/C composites were prepared by annealing of the as-obtained ZnGly in a tube furnace at different temperatures between 400 and 800 °C for 2 h under N_2 flow at an initial heating rate of 5 °C min^{-1}. The carbonized products are termed as ZnO/C-X, where X is the annealing temperature. For the purpose of comparison, a bare ZnO sample was prepared by annealing of the ZnO/C-800 composite at 600 °C for 1 h in air.

Materials characterization

The synthesized ZnO/C-X composites were characterized by a variety of complementary experimental techniques, as described in detail below. X-ray diffraction (XRD) patterns were obtained with a Bruker AXS D8 Advance Eco diffractometer using Cu K_α radiation and a step size of $\Delta(2\theta) = 0.02°$ at the angular scan. The morphology of the samples was investigated using a ZEISS Leo 1530 scanning electron microscope (SEM) and a JEOL JEM 2100 transmission electron microscope (TEM). Raman spectra of the samples were recorded on a Bruker Senterra spectrometer equipped with Olympus BX-51 optical microscope using a 532 nm laser. To avoid damage to the samples, the emitted power was limited to 2 mW. All spectra were obtained at room temperature at a wavelength range from 100 to 4000 cm^{-1} using a 400 lines mm^{-1} grid and 25 × 1000 μm aperture. X-ray photoelectron (XP) spectra of the samples were measured with MAX200 (Leybold-Heraeus) spectrometer equipped with a non-monochromatized Mg $K\alpha$ X-ray source (200 W) and a hemispherical analyzer. The powder materials were pressed into clean indium foil and thinned by a brush to suppress charging effects, following the established methodology [28]. Thermogravimetric analysis (TG/DTA) was performed on a Mettler Toledo TGA/DSC1 analyzer with a heating rate of 5 °C min^{-1} in air and Ar. The content of carbon was examined by elemental analysis using Vario MICRO Cubes (Elementar). Nitrogen sorption isotherms were determined on a Micromeritics Gemini VII 2390 Surface Area Analyzer. Prior to N_2 physisorption data collection, the samples were degassed at 150 °C under vacuum for 4 h. The specific surface area, pore size distribution, and pore volumes were obtained by means of the Brunauer–Emmett–Teller (BET) method and the Barrett-Joyner-Halenda model from the adsorption branches of the isotherms.

Electrochemical measurements

Electrochemical studies were performed in Swagelok-type two electrode cells at 25 °C by using a VMP3 potentiostat (Bio-Logic SAS) (see [26]). The preparation procedure of the working electrodes is as follows. A mixture of 80% ZnO/C, 15% carbon black (Super C65, Timcal), and 5% polyvinylidene fluoride binder (PVDF, Solvay Plastics) dissolved in N-methyl-2-pyrrolidone (NMP, Sigma-Aldrich) was stirred for at least 12 h. In order to obtain a spreadable slurry most of the NMP was evaporated in a vacuum oven (10 mbar, 65 °C). The resulting electrode slurry was applied on circular Cu meshes (diameter 10 mm) with a mass loading of about 2 mg cm^{-2}. Afterward, the electrodes were dried at 80 °C under vacuum, mechanically pressed at 10 MPa, and then dried again. The working electrode and the counter electrode, consisting of a lithium metal foil disk (Alfa Aesar) pressed on a nickel current collector, were separated by two layers of glass fiber separator (Whatman GF/D). As electrolyte 200 μL of a 1 M LiPF$_6$ salt solution in 1:1 ethylene

carbonate (EC) and dimethyl carbonate (DMC) (Merck Electrolyte LP30) was used. The cells were assembled in a glove box under argon atmosphere ($O_2/H_2O < 5$ ppm). For *ex-situ* XRD measurements the cells were galvanostatically cycled at 10 mA g^{-1} and disassembled at various dis-/charged states in the glove box. The electrodes were washed in DMC and dried under vacuum conditions overnight. The XRD measurement of the post-cycled electrode material was performed using an airtight sample carrier.

Results and discussion

The structure of the ZnO/C-X composites was analyzed by XRD (Fig. 1a). For comparison, the XRD pattern of ZnO obtained by annealing the ZnO/C-800 composite in air at 600 °C is also included. All diffraction peaks can be assigned to a hexagonal phase of wurtzite-type ZnO according to JCPDS # 36–1451, space group P63mc. Lattice parameters determined by means of full-profile analyses with the FullProf Suite (see Table 1) are in good agreement with the literature. The intensities of the characteristic peaks of ZnO increase with rising annealing temperatures. For ZnO/C composites prepared by heat treatment below 600 °C, the diffraction peaks are rather broad which is attributed to nanosized ZnO crystallites. The crystallite sizes of ZnO in the ZnO/C-X (X = 400, 500, 600) samples are calculated using the Scherrer equation:

$$D_{hkl} = K\lambda/\Delta(2\theta_{hkl})\cos\theta_{hkl}, \tag{3}$$

where D_{hkl} is the average grain size based on the particular reflecting crystal face (*hkl*) direction, K is a shape factor which can be approximated to 0.9, λ is the wavelength of the applied Cu Kα radiation, $\Delta(2\theta_{hkl})$ is the full width at half-maximum of the diffraction peak and θ_{hkl} is the Bragg angle. The analysis of the peaks below $2\theta_{hkl} = 65°$ yields the averaged crystallite size for the ZnO/C-X samples. Both, ZnO/C-400 and ZnO/C-500 composites, exhibit similar particle size of around 12 nm. By contrast, the ZnO/C-600 composite is characterized by a larger size of 19 ± 3 nm.

Raman spectra collected from the ZnO/C-X (X = 400 − 700) samples display two prominent peaks which are attributed to the carbon D- and G-bands (see Fig. 1b). The G-band corresponds to sp^2-bonded carbon atoms, while the D-band is associated with defects or disorders mainly due to sp^3 hybridization [29]. The D- and G-bands of the ZnO/C-400 composite are located at 1359 cm^{-1} and 1591 cm^{-1}, respectively. In comparison, the D-and G-peaks of the ZnO/C-700 sample are slightly red-shifted by 23 and 20 cm^{-1} toward 1314 and 1571 cm^{-1}, respectively. The same shift toward higher binding energy indicating the strong chemical interaction between the surface carbon and Zn atoms was observed by XPS on ZnO/C composite [23]. Similar shifts have been reported for TiO$_2$/C composites [30, 31]. These shifts are attributed to the stress induced by the chemical anchoring of ZnO atoms on the carbon surface. Obviously, such an interaction can change the Raman shifts describing the carbon bond energy. The ratio of the maximum intensities, I_D/I_G, was calculated as 0.73 and 0.91 for
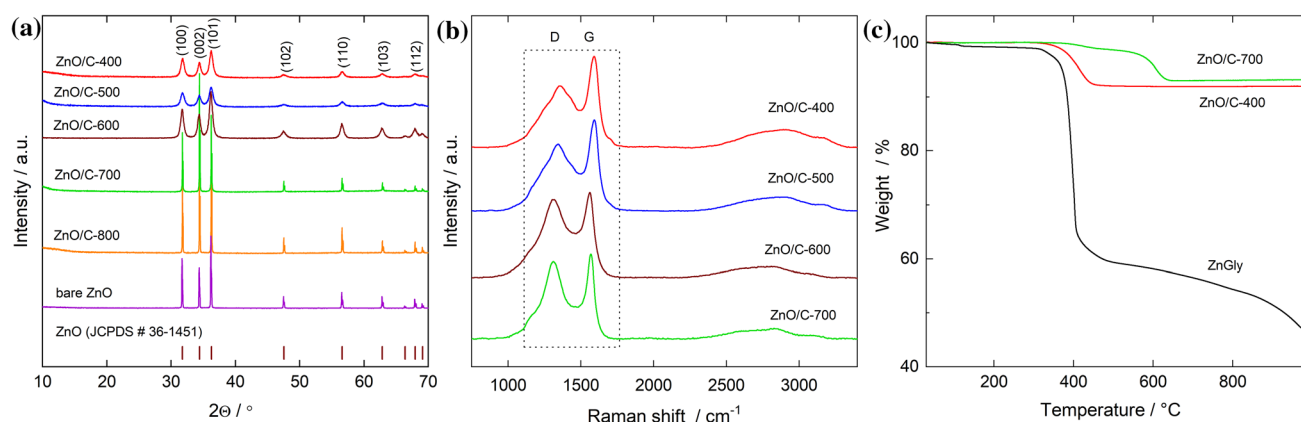
Figure 1 **a** XRD patterns and **b** Raman spectra of the ZnO/C-X composites and bare ZnO sample as well as (**c**) TG curves for the ZnGly precursor heated in an inert atmosphere and ZnO/C-400(700) composites heated in air.

Table 1 Lattice parameters obtained from Rietveld refinement, results of BET analysis, and carbon content for the ZnO/C-X composites and bare ZnO

| Sample	Lattice parameters		S_{BET} (m g^{-1})	Total pore volume (cm^3 g^{-1})	Carbon content (wt%)	
	a (Å)	c (Å)			TG	Chemical analysis
ZnO/C-400	34.80	52.05	54.8	0.18	8.0	8.7(5)
ZnO/C-500	32.49	52.06	59.8	0.16	7.1	8.2(5)
ZnO/C-700	32.55	52.16	100.9	0.36	5.7	6.0(5)
ZnO/C-800	32.53	52.11	93.1	0.29	–	5.8(5)
ZnO	32.49	52.05	6.6	0.02	–	–

the ZnO/C-400 and ZnO/C-700 composite, respectively. According to the model proposed by Ferrari and Robertson, the ratio I_D/I_G is proportional to the crystallite size, when it is less than 2 nm for amorphous carbon [32]. The increasing intensity of the D-band with rising annealing temperature is characteristic of the carbonization process and implies less disorder and a lower number of defects in the carbon component due to a growing crystallite size [33, 34]. The peaks associated with ZnO were not observed by Raman spectroscopy using a laser wavelength of 532 nm.

TG/TGA analysis (Fig. 1c) of the ZnGly precursor illustrates its conversion into carbon containing zinc oxide upon annealing in a nitrogen atmosphere. A significant weight loss of ca. 40% at heating from 400 to 1000 °C can be explained by the total decomposition of the ZnGy precursor with simultaneous formation of zinc oxide, volatile products with low molecular weight and products of condensation of organic compounds, similar to titanium glycerolate [26]. Furthermore, the products of the condensation also undergo a disproportionation with the formation of volatile low molecular weight substances and the carbonaceous part of the ZnO composite. Therefore, 400 °C was selected as the start reaction temperature to calcine the ZnGly precursor under nitrogen environment to produce the ZnO/C composites. The carbon content in the as-prepared ZnO/C-X composites was determined by the TG/TGA measurements in air, performed in the temperature range up to 1000 °C to ensure the complete oxidation of carbon into carbon dioxide (cf. Table 1). As a result, the carbon contents in the ZnO/C-400 and ZnO/C-700 composites were estimated at 8.0 and 5.7 wt%, respectively. These values were additionally verified by the chemical analysis, with good agreement of the results (Table 1).

To confirm the formation of the ZnO/C composites and to exclude other oxidation states of Zn, XPS analyses were carried out on ZnO/C-400 and ZnO/C-700. The XPS survey spectrum and core level spectra of the Zn 2p, O 1 s and C 1 s peaks for both samples are shown in Fig. 2. The survey spectrum in Fig. 2a displays the presence of Zn, O, C without any detectable impurities. The Zn 2p spectra of both samples in Fig. 2b exhibit a single Zn 2p$_{3/2,1/2}$ doublet, with the positions of the Zn 2p$_{3/2}$ and Zn 2p$_{1/2}$ components, 1021.6 eV and 1044.7 eV, respectively, corresponding to Zn^{2+} [11, 23]. This assignment is additionally supported by the kinetic energy position of the most intense Zn LMM Auger peak at 988 eV (Fig. S1), which corresponds to ZnO. The O 1 s spectrum, as shown in Fig. 2c, was resolved and the lower binding energy component at 530.7 for the ZnO/C-400 sample and 530.6 eV for the 700 sample can be attributed to the hexagonal close packing of O$_2$ in the wurtzite-ZnO structure. The peak at 532.3 eV for both samples is associated with surface hydroxyl groups (OH) and/or C=O. The peak at 533.9 and 534.2 eV corresponds to single bonds between oxygen and carbon (C-O) and/or absorbed water [35]. The C 1 s spectra, which are shown in Fig. 2d, can be fitted by four sub-peaks, the aliphatic C–C, the C–O, C=O, and O–C=O peak [35]. For ZnO/C-400 the positions of these peaks are at 284.8, 286.2, 287.9, and 289.9 eV and for ZnO/C-700 the peaks are located at 284.4, 286.6, 287.9, and 289.8 eV. The shift of the C–C peak from ZnO/C-400 to ZnO/C-700 towards lower binding energies indicates, in accordance with the Raman data, a more graphitic state for the carbon component of the ZnO/C-700 composite [36].

Figure 2 XPS spectra of ZnO/C-400 and ZnO/C-700: **a** survey spectrum, **b** Zn 2p, **c** O 1 s and **d** C 1 s.
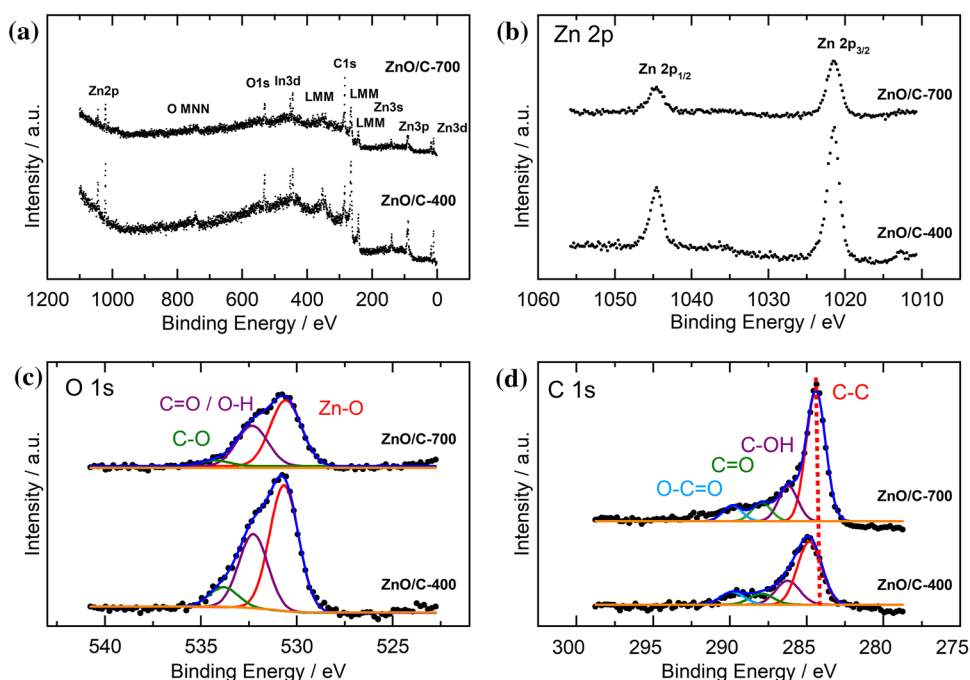

SEM images of the ZnO/C-X composites in Fig. 3 show the drastic effect of the calcination temperature on the morphology of the samples. The pristine ZnGly precursor is mainly composed of irregularly shaped sheets with several micrometers in length (Fig. 3a). The ZnO/C composites fabricated via annealing of the precursor at a temperature below 500 °C consist of sheets with an average size of few micrometers, which are primarily composed of nanosized grains of ZnO (Fig. 3b, c). Probably, carbon acts as a cross-linking agent that holds the ZnO nanoparticles together. The cross-sectional SEM images of the sheets show that their thickness changes from 270 to 800 nm for ZnO/C-500 and ZnO/C-400 composites, respectively (Fig. 3b, c, insert). In contrast, the ZnO/C-700 and ZnO/C-800 composites consist of many thin sheets and several large particles of about 1 − 7 μm in diameters (Fig. 3d, e). As shown in Fig. 3f, the bare, carbon-free ZnO particles, obtained by the heat treatment of the ZnO/C-800 composite in air, represent hexagonal ZnO prisms with an average size of about 1–7 μm.

Further information on the morphology and structural features of the sheets in the ZnO/C-700 composite was obtained by TEM studies. The TEM images shown in Fig. 4a exhibit well crystallized ZnO nanoparticles which are dispersed in a carbon matrix. The corresponding high-resolution TEM (HRTEM) image in Fig. 4b exhibits lattice fringes with spacings

of 0.26 and 0.28 nm, which correspond to the distances between the (002) and (100) planes of ZnO, respectively. Furthermore, the crystalline structure of the ZnO/C-700 composite is confirmed through the selected area electron diffraction (SAED) pattern as shown in Fig. 4c. Several clear diffraction rings from the SAED pattern can be assigned to the (100), (002), (101), (102), (110), (103), and (200) planes of hexagonal ZnO, suggesting a polycrystalline nature of the ZnO component in the composite.

The porous nature and the specific surface area of the as-prepared samples were investigated by nitrogen adsorption–desorption isotherms. Corresponding pore size distribution plots of the samples are shown in Fig. 5. The ZnO/C-X composites display isotherms of type IV, according to the IUPAC classification, with a H3 hysteresis loop (Fig. 5a) [37]. The isotherms of the bare ZnO powder are close to type II, which is typical for non-porous or macroporous materials. The BET specific surface area and the respective pore volumes of the samples are displayed in Table 1. The BET surface area of the ZnO/C-X composites is rather high which is attributed to the presence of mesopores, in contrast to the bare ZnO which displays a very low value of this parameter (6.7 $m^2 g^{-1}$). In the case of the ZnO/C-X hybrid materials, the annealing temperature of the ZnGly precursor affects the specific surface area significantly as this parameter increases with the increasing

Figure 3 SEM images of (**a**) ZnGly precursor, **b** ZnO/C-400, **c** ZnO/C-500, **d** ZnO/C-700, **e** ZnO/C-800 composites, and **f** bare ZnO sample. Insets show high-magnification SEM images of cross sections of ZnO/C-400(500) composites.
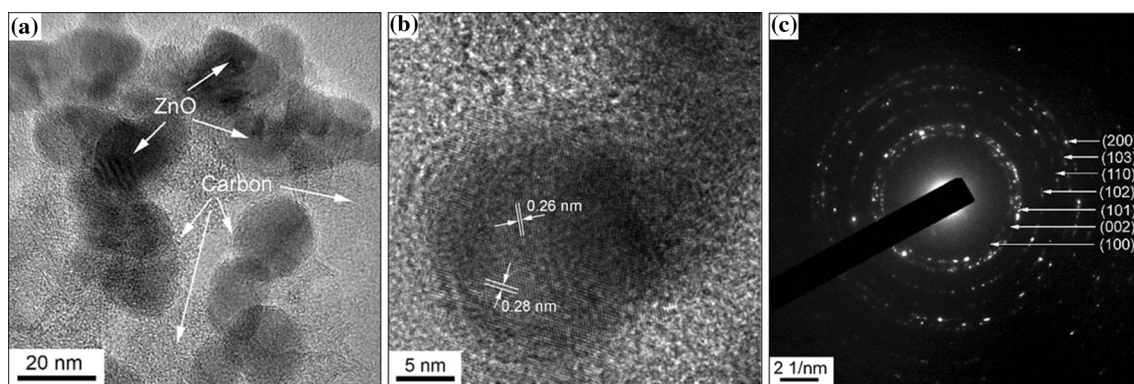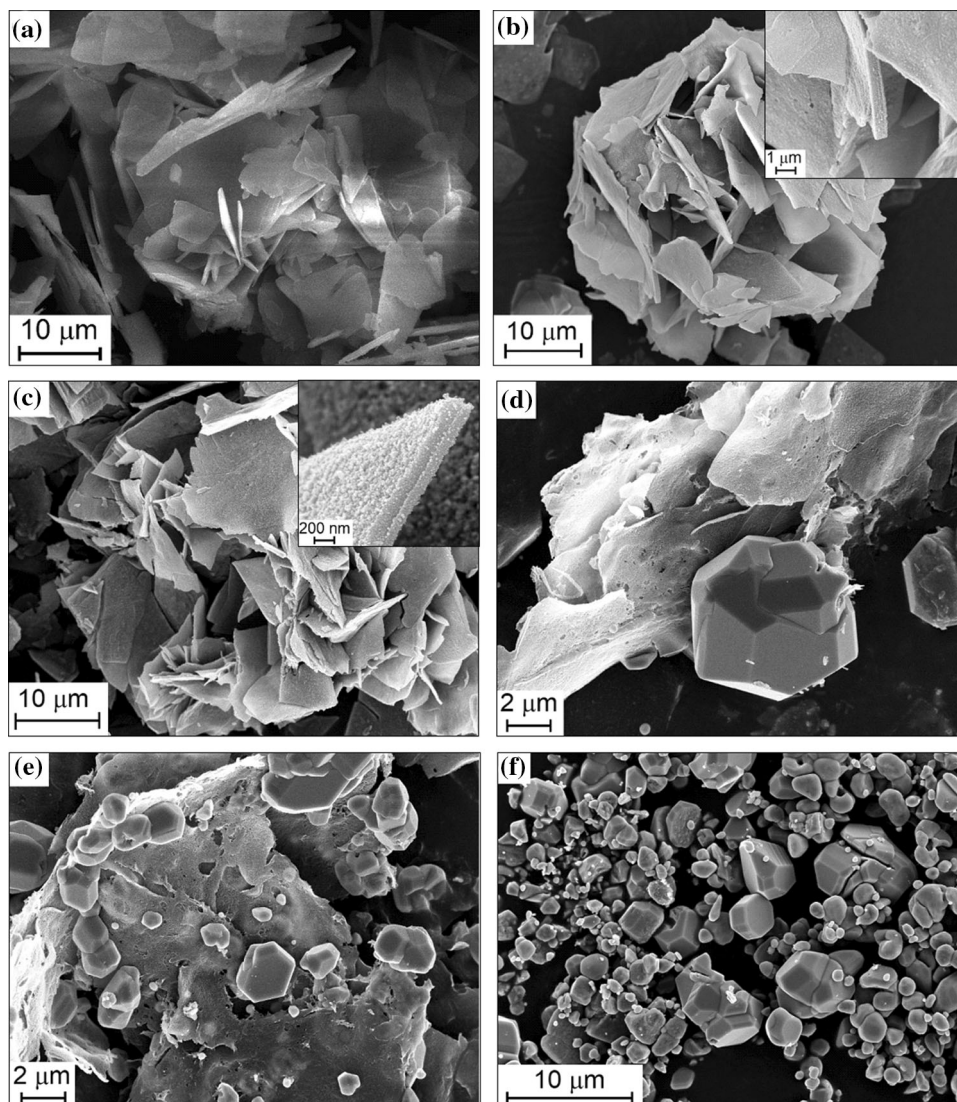

Figure 4 **a** TEM image, **b** HRTEM image, and **c** SAED pattern of ZnO/C-700 composite.

annealing temperature, from 400 to 700 °C. We attribute this behavior to the formation of defects in the composite structure during their annealing under

N_2. The decrease in the specific surface area of the ZnO/C-800 composite compared to the ZnO/C-700 composite is attributed to the appearance of large
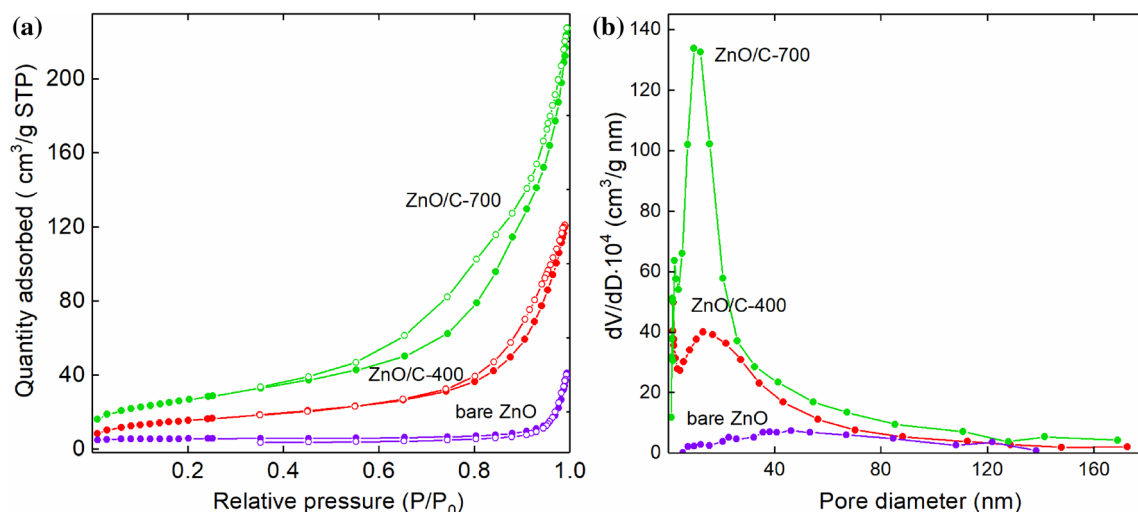
Figure 5 **a** N2 adsorption–desorption isotherms and **b** BJH pore size distribution curves of as-prepared ZnO/C composites and bare ZnO powder.

ZnO particles, as demonstrated by the SEM images (Fig. 3). Note, the ZnO/C-700 composite shows the highest BET surface of 100.9 m^2 g^{-1}. From the pore size distribution plots (Fig. 5b), it is obvious that mesoporous structures are predominant in the fabricated ZnO/C-X composite materials.

The fabricated hybrid nanomaterials were studied with respect to their applicability as electrode materials in LIBs. Note, that the mesoporous nature of these materials is supposed to facilitate penetration of the electrolyte, thereby securing good electrical contact with the electrode and accelerating the diffusion kinetics. The electrochemical properties were investigated by cyclic voltammetry (CV) and galvanostatic cycling with potential limitation (GCPL). Figure 6a shows the first, second, third and tenth CV cycles for the ZnO/C-400 composite at a scan rate of 0.1 mV s^{-1} in a voltage range of 0.01–3.0 V. During the first reductive sweep the irreversible formation of the solid electrolyte interphase (SEI) occurs at around 0.6 V (R3). The peak R1 at the lower voltage limit of 0.01 V originates in part from the lithiation process related to carbon [38]. Since no corresponding oxidative peak is visible, we conclude that the delithiation process takes place over an extended voltage range. The reduction peak R2 and the oxidation peaks O1–O4 can be assigned to the Li$^+$ storage in ZnO [5, 6]. In the initial scan the reduction peak R2 at 0.3 V can be ascribed to both electrochemical reactions, the conversion and the alloying process [6]. After the second cycle R2 splits up in R2$_A$ (0.4 V) and R2$_C$ (0.7–0.8 V) which may be explained

by a reduced overpotential of the conversion reaction at R2$_C$ due to structural changes during the initial cycle as compared to the conversion reaction at R2 while the alloying reaction at R2$_A$ is not significantly affected. Such a behavior is also observed for other conversion materials, such as Mn$_3$O$_4$ [38]. The oxidation peaks O1–O3 located between 0.3 and 0.7 V are assigned to the dealloying of LiZn alloy. The occurrence of several peaks suggests a multi-step process with various LiZn intermediate stages, such as Li$_2$Zn$_3$, LiZn$_2$ and Li$_2$Zn$_5$ [39, 40]. The peaks O1–O3 as well as R2$_A$ corresponding to the alloying process show good cycling stability. The oxidation feature O4 at around 1.3 V finally signals conversion to ZnO [6, 9]. Upon further cycling, the redox peak pair R2$_C$/O4 quickly decreases in intensity indicating an inactivation of the conversion reaction of ZnO Eq. (1). In contrast to the CV curve of the ZnO/C-400 composite, in case of the ZnO/C-700 composite (Fig. 6b) and bare ZnO (Fig. 6c) the oxidation peaks O1—O4 have lower intensity in the first cycle, while an additional oxidation peak at 2.6 V, labeled as O5, can be observed. The latter feature was also observed in several previous studies [3, 6, 7, 41, 42] but its origin still remains unclear. Huang et al. [3] and Pelliccione et al. [6] have speculatively assigned it to the back formation of ZnO Eq. (2) and the oxidation peak O4 to the dealloying process Eq. (1). In contrast, Mueller et al. [7] showed by means of *in-situ* XRD studies that the dealloying process is completed even before the oxidation process O4 starts and that ZnO is formed only afterwards, at O4. However, while these
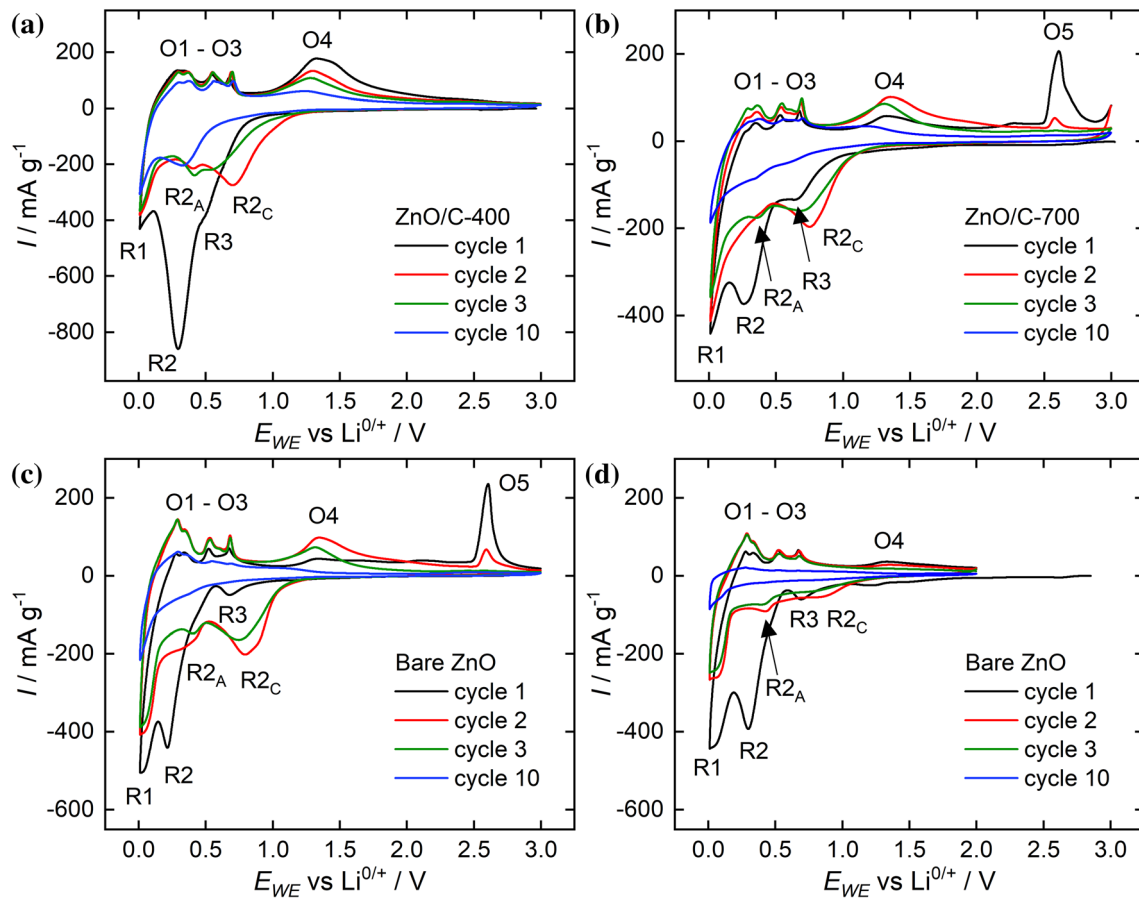
Figure 6 Cyclic voltammograms of (**a**) ZnO/C-400, **b** ZnO/C-700, and bare ZnO in the range of **c** 0.01–3 V and **d** 0.01–2 V at a scan rate of 0.1 mV s^{-1}. O1–O5 and R1–R4 label oxidation/reduction features as discussed in the text.

results exclude the above-mentioned assignment of O5, Mueller et al. make no further statements about this oxidation process. Hence, for understanding of the latter process we recorded a CV of the bare ZnO anode in a restricted potential range of 0.01–2.0 V (Fig. 6d), excluding O5. The comparison of this CV curve with the full range scans shows that the electrochemical activity steadily and strongly decreases in case of O5 exclusion, whereas otherwise, i.e., when the oxidation O5 takes place, the intensities of the subsequent features are significantly higher. Apparently, the oxidation process O5 plays a decisive role in the reversibility of Li$^+$ storage processes.

Ex-situ XRD measurements were performed in order to get insight into the structural changes of ZnO/C composites during electrochemical cycling. The XRD patterns of the ZnO/C-700 electrode at different dis-/charge states are shown in Fig. 7. In the initial state, the hexagonal ZnO phase (JCPDS #36–1451) is identified. The additional peaks at 44°

and 51° originate from the Cu current collector. After discharging to 0.6 V the XRD pattern is similar to that of the as-prepared electrode. As expected, this implies that the electrode material does not undergo any structural transformation during the SEI formation. By further discharging to 0.3 V, the hexagonal ZnO phase completely transforms into a Zn phase (COD #9,008,522), which goes along with the conversion reaction according to Eq. (1). As can be seen from the expanded view of the 27–41° 2θ range in the inset of Fig. 7, a broad low intensity peak located at 33.7° indicates the presence of Li$_2$O (ICSD #54,368). It can be observed for all the following charge states as exemplarily shown by the XRD patterns of the fully charged and discharged state in the inset of Fig. 7. The XRD pattern of the completely discharged electrode (i.e., at 0.01 V) exhibits the characteristics of a single LiZn phase (COD #1,539,519), resulting from the alloying process described by Eq. (2). The observed structural changes upon cycling are in good
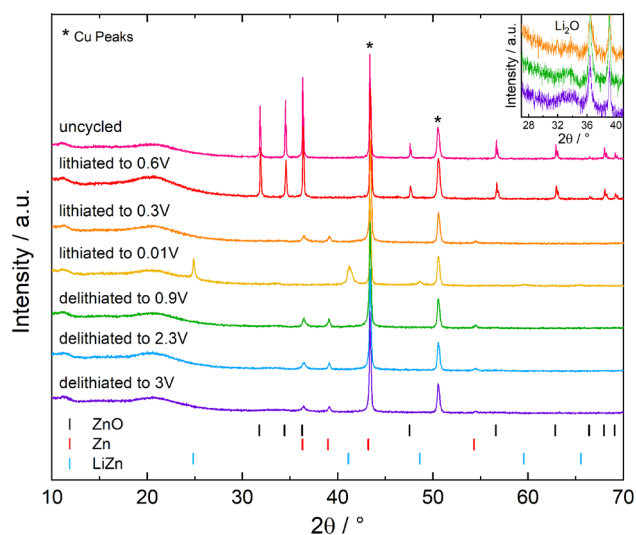
Figure 7 *Ex-situ* XRD patterns of a ZnO/C-700 electrode recorded at different stages of electrochemical Li⁺ de-/insertion. The reflexes marked with * originate from the Cu current collector. In addition, the Bragg peak positions for ZnO (JCPDS # 36–1451), Zn (COD #9,008,522), and LiZn (COD #1,539,519) are shown. The inset shows the expanded view of XRD patterns of the samples lithitated up to 0.01 V (fully discharged), 0.9 V, and 3 V (fully charged) in the 27–41° 2θ range.

agreement with the reported results for a two-step mechanism for Li⁺ storage in ZnO including a conversion and an alloying process [5, 40]. During the subsequent charging to 0.9 V, the peaks associated with LiZn vanish and the Zn phase reappears, confirming the reversibility of the alloying process. As charging proceeds to 3 V, the peaks associated with the Zn phase diminish in intensity, while no other crystalline phase shows up. Apparently, no structural changes are associated with the oxidation processes reflected by O4 and O5. Against expectation, there is no indication of crystalline ZnO in the completely charged electrode (i.e., at 3 V). This might be explained either by the amorphous structure or nanosize of the electrochemically formed ZnO or by the irreversibility of the conversion reaction Eq. (1). The lattice parameters of the Zn and LiZn phases appearing at various charging stages during the electrochemical cycling were determined by means of full-profile analyses with the FullProf Suite (Table S1). *Ex-situ* XRD studies on ZnO/C-400 show similar results (Fig. S2).

GCPL measurements at a current density of 100 mA g⁻¹ in the range of 0.01–3.0 V enable assessing the cycling performance of the composite
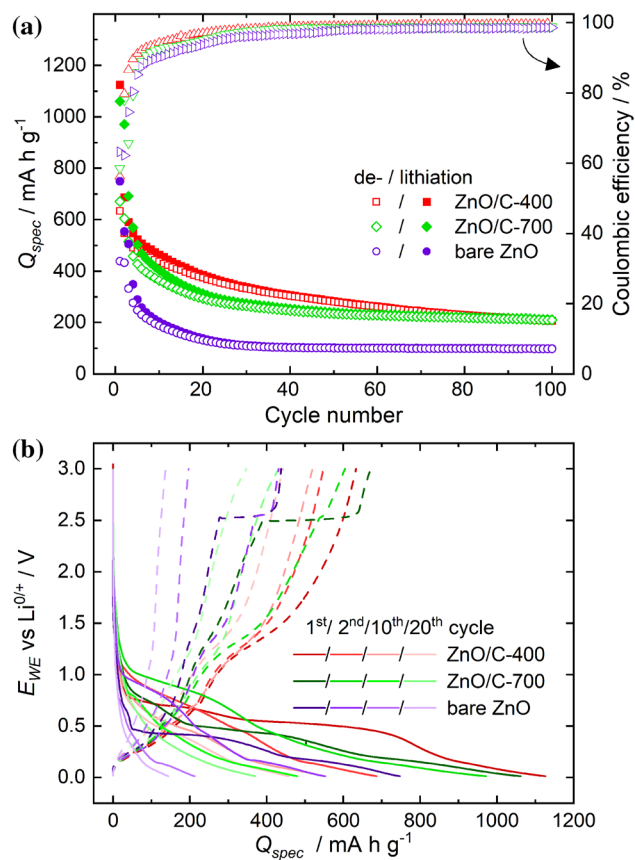

Figure 8 a Specific dis-/charge capacities and coulombic efficiencies of the ZnO/C-400 and ZnO/C-700 composites and of bare ZnO for galvanostatic cycling in the potential range between 0.01 and 3 V at 100 mA g⁻¹ as well as (**b**) the respective potential profiles for the first, second, tenth and twentieth cycles.

nanomaterials under study. Figure 8a shows specific dis-/charge capacities and coulombic efficiencies for the first 100 cycles of the ZnO/C-400 and ZnO/C-700 composite as well as of the bare ZnO electrode. In the first cycle specific dis-/charge capacities of 1126/633 mAh g⁻¹ (ZnO/C-400), 1061/671 mAh g⁻¹ (ZnO/C-700) and 749/439 mAh g⁻¹ (ZnO) were measured. One reason for the large capacity loss in the first cycle is the irreversible SEI formation during discharge. As can be seen from the potential profiles of the first lithiation (Fig. 8b), for bare ZnO the SEI contribution is quite small with less than 50 mAh g⁻¹, whereas for the composites it is larger due to the fact that the irreversible charge loss is roughly linearly proportional to the specific surface area of carbonaceous materials [43]. Cracking and fracture of the electrode material due to large volume changes can lead to an unstable SEI and irreversible capacity losses beyond

the first cycle [44], which also might explain the unexpected high second discharge capacity of ZnO/C-700 compared to the first charge capacity. Based on the reaction mechanism of ZnO Eqs. (1) and (2), a maximal theoretical specific capacity of 978 mAh g^{-1} can be reached. Considering the capacity from the SEI formation, it can be concluded that in the case of the composites the ZnO almost fully reacts with Li$^+$ according to the expected reaction mechanism, while this is not the case for the bare ZnO electrode. After 20 cycles 293 mAh g^{-1} can be charged from ZnO/C-700 and a slightly higher capacity of 374 mAh g^{-1} from ZnO/C-400, corresponding to a capacity fading of 44% and 41% relative to the first cycle. The poor coulombic efficiencies and rapid capacity fading during the first twenty cycles might be explained by the limited reversibility of the conversion reaction Eq. (1). This is supported by the results of *ex-situ* XRD studies. Under the assumption that the back formation to ZnO Eq. (1) is irreversible and the reversible lithiation reaction is a single alloying process Eq. (2) a maximal capacity of only 329 mAh g^{-1} can be expected. Obviously, the charge capacities exceed this value for about the first twenty cycles indicating that the reoxidation of Zn to ZnO is at least partly reversible as also observed by Pelliccione et al. [6] and Mueller et al. [7]. Interestingly, during further cycling the coulombic efficiencies are increasingly converging at 100% and simultaneously the cycling stabilities get much better. Exemplarily, the ZnO/C-700 composite delivers a discharge capacity of 212 mAh g^{-1} after 100 cycles exhibiting excellent cycle stability with an average capacity loss of only 0.04% per cycle over the last 80 cycles. The potential profiles of the first, second, tenth and twentieth cycle in Fig. 8b provide an insight into the origins of the capacity fading. Comparing the potential profiles, it is noticeable that the capacity loss can be mainly traced back to an inactivation of the conversion reaction Eq. (1), which can also be observed in the CV curves (Fig. 6). During the first cycles both processes, viz. the conversion and the alloying, take place but in the further course the alloying mainly contributes to the Li$^+$ storage, which might be due to the incomplete back formation of ZnO. In addition, the loss of electrical connectivity to the active material due to changes in the electrode structure, such as particle aggregation or pulverization, results in capacity losses. Comparing the two composites, indeed, the capacities of the ZnO/C-700 composite fade more

rapidly in the first cycles with lower coulombic efficiency than for ZnO/C-400 but stabilize faster in the further course. It should be noted, that the evolution of the capacities of the ZnO/C-500 sample is similar to that of ZnO/C-400 while the evolution of the capacities of the ZnO/C-800 sample is similar to that of ZnO/C-700 (Fig. S3), who each have similar crystallographic and morphological properties, respectively. The worse cycling stability of the ZnO/C-700 composite in the first twenty cycles might be attributed to the presence of microscaled polyhedrons, whereas the ZnO/C-400 composite consists only of nanoscaled primary particles. For one thing, the reversibility of the conversion reaction depends on the crystallite size of the transition metal particles formed during electrochemical cycling [45]. Park et al. [9] have shown that the back formation of ZnO
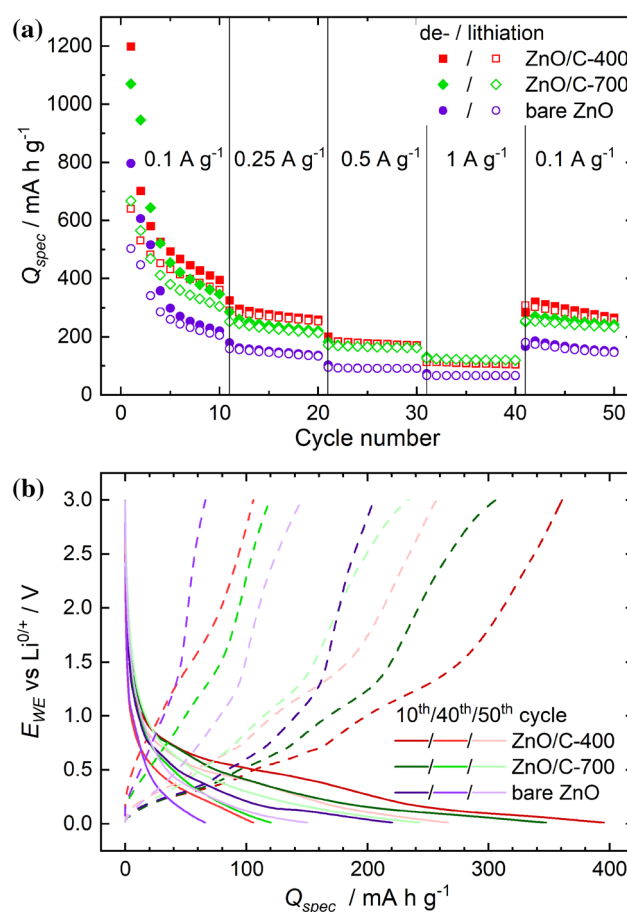
Figure 9 a Rate capability test of the ZnO/C-400 and ZnO/C-700 composites and of bare ZnO at current rates between 100 and 1000 mA g^{-1} as well as (b) the respective potential profiles of cycle 10 at 100 mA g^{-1}, cycle 40 at 1000 mA g^{-1} and cycle 50 again at 100 mA g^{-1}.

only occurs for extremely small Zn nanocrystallites. In addition, nanosized particles can better accommodate the strain caused by the volume changes during electrochemical cycling [46]. Looking at the comparison between the ZnO/C composites and the bare ZnO sample, it is remarkable that over the whole measurement the composites reach about twice the capacities of the bare sample. In cycle 20 and 100, the bare ZnO compound reaches specific capacities of 131 mAh g^{-1} and 97 mAh g^{-1}, respectively. The higher capacities of the composite materials can be probably traced back to the larger surface area offering more active sides as well as a better electronic connection of the ZnO particles due to the conductive network provided by the carbon. Furthermore, the stabilized coulombic efficiency and the cycling stability of the bare ZnO electrode is with a capacity loss of 70% in cycle 20 relative to the first cycle worse than for the composites. We conclude that degradation effects such as structural changes of the electrode material leading to the electrical disconnection of the active material as well as an unstable SEI can be at least partly prevented by the carbon. The carbon matrix can effectively suppress the nanoparticle aggregation and pulverization of the electrode material due to large volume changes maintaining the structural stability and, moreover,

helping stabilize SEI formation [23, 47–49]. In addition, the electrochemical properties of bare ZnO and the ZnO/C-400 and ZnO/C-700 composites were also investigated by galvanostatic cycling with various current densities between 100 and 1000 mA g^{-1}. The specific dis-/charge capacities are shown in Fig. 9a along with the potential profiles of cycle 10 at 100 mA g^{-1}, cycle 40 at 1000 mA g^{-1} and cycle 50 again at 100 mA g^{-1} in Fig. 9b. The ZnO/C-400 composite reaches a charge capacity of 113 mAh g^{-1} at a high current rate of 1000 mA g^{-1} while for ZnO/C-700 a charge capacity of 125 mAh g^{-1} is measured and for bare ZnO 67 mAh g^{-1}. The inferior rate capability of the sample ZnO/C-400 compared to ZnO/C-700 is caused by a more severe polarization resistance due to kinetic effects. As can be seen from the potential profiles, at a high current rate of 1000 mA g-1, the potential gap between charge and discharge increases more for ZnO/C-400 than for ZnO/C-700. The reduced polarization resistance in case of ZnO/C-700 might be associated with better conductivity of the less disordered carbon as shown by Raman spectroscopy and the XPS analysis. When the current density is reset to 100 mA g^{-1} charge capacities of ca. 83%, 86% and even 88% relative to cycle 10 can be regained for the ZnO/C-400, ZnO/C-700 and bare ZnO samples, respectively.

Table 2 Comparison of the electrochemical performance of ZnO and ZnO/C electrodes prepared via different synthesis methods as reported in the literature

Sample	Method of synthesis	Current density (mA g^{-1})	Discharge capacity (mAh g^{-1})/cycle no	References
ZnO spheres	Hydrothermal	100	109/100	[2]
ZnO/C nanoparticles	Thermal decomposition of Zn$_3$(C$_6$H$_5$O$_7$)$_2$	100	850/200	[22]
ZnO/C spheres	Thermal decomposition of Zn$_3$(C$_6$H$_5$O$_7$)$_2$	100	520/150	[24]
ZnO/C nanoparticles	Thermal decomposition of C$_4$H$_4$ZnO$_6$	100	610/300	[25]
ZnO/C nanocages	Pyrolysis	100	750/100	[50]
ZnO/C spheres	Pyrolysis	100	750/100	[51]
ZnO/C nanoparticles	Ball milling	100	610/500	[52]
ZnO/C tetrahedron	Calcination	110.7	518/300	[53]
ZnO/C nanoparticles	Calcination	100	610/50	[54]
ZnO/C spheres	Coprecipitation	500	659/300	[55]
ZnO/C-400	Thermal decomposition of ZnC$_3$H$_6$O$_3$	100	208/100	This work
ZnO/C-700		100	212/100	
ZnO		100	98/100	

Interestingly, the comparison with the measurement consistently at 100 mA g^{-1} (Fig. 8) reveals that the capacity fading seems to be more serious for electrochemical cycling at lower rates accompanied with higher Li$^+$ storage capacity. For ZnO/C-400, ZnO/C-700 and bare ZnO which were continuously cycled at 100 mA g^{-1}, charge capacities of only 68%, 67% and 54% were obtained in cycle 41 relative to cycle 10. Higher degradation effects for a more comprehensive dis-/charge process might be explained as a result of more serious structural damages of the electrode material. For comparison purposes, Li storage performance of the as-prepared ZnO/C anodes and those of ZnO and ZnO/C materials reported in literature are summarized in Table 2. The results show that the cycling performance of ZnO/C composites compared with bare ZnO is much better owing to positive effects of carbon. The differences of the specific capacities of ZnO/C composites produced by various methods can be attributed to the morphology, crystal size, specific surface area as well as porosity which influence the electrochemical properties of the electrode materials. The lower electrochemical activity of the ZnO/C composites in this work compared to most of ZnO materials in literature can be explained by their morphological features and carbon content in the compounds. The as-prepared composites are composed of ZnO particles with relatively large dimensions. Small-sized particles have a large surface area, which provides more active sides resulting in high specific dis-/charge capacities. The good electrochemical performance of the electrodes prepared by the thermal decomposition of the different organometallic complexes [22, 24, 25] can be attributed to the distinctive carbon content in the products.

Conclusions

In conclusion, a facile method to synthesize ZnO/C composites, involving a thermal treatment of zinc glycerolate as a source of both carbon and zinc, was demonstrated. This one-pot method allows the synthesis of a variety of controllable ZnO/C composites with distinctive nano/microscaled arrays of ZnO particles. When used as anode material for lithium-ion batteries, the ZnO/C composite synthesized at a calcination temperature of 700 °C achieves high initial discharge and charge capacities of 1061 and 671 mAh g^{-1} at a current rate of 100 mA g^{-1}. As compared to the bare ZnO, the composites exhibit significantly better electrochemical properties, such as higher specific capacities and superior cycling stability. The carbon acts as a conductive network that runs through the material leading to the prevention of inactive areas and thus to a higher electrochemical activity. *Ex-situ* XRD studies confirm a two-step mechanism for lithiation of ZnO including a conversion and alloy process.

Declarations

Conflict of interest The authors declare that they have no conflict of interest.

Supplementary Information: The online version contains supplementary material available at http s://doi.org/10.1007/s10853-021-06125-4.

References

[1] Wang Y, Deng Q, Xue W, Jian Z, Zhao R, Wang J (2018) ZnO/rGO/C composites derived from metal–organic framework as advanced anode materials for Li-ion and Na-ion batteries. J Mater Sci. https://doi.org/10.1007/s10853-018-2003-3

[2] Wu G, Jia Z, Cheng Y, Zhang H, Zhou X, Wu H (2019) Easy synthesis of multi-shelled ZnO hollow spheres and their conversion into hedgehog-like ZnO hollow spheres with superior rate performance for lithium ion batteries. Appl Surf Sci. https://doi.org/10.1016/j.apsusc.2018.09.115

[3] Huang XH, Guo RQ, Wu JB, Zhang P (2014) Mesoporous ZnO nanosheets for lithium ion batteries. Mater Lett. https://doi.org/10.1016/j.matlet.2014.02.012

[4] Kundu S, Sain S, Yoshio M, Kar T, Gunawardhana N, Pradhan SK (2015) Structural interpretation of chemically synthesized ZnO nanorod and its application in lithium ion battery. Appl Surf Sci. https://doi.org/10.1016/j.apsusc.2014.12.152

[5] Fu Z-W, Huang F, Zhang Y, Chu Y, Qin Q-Z (2003) The electrochemical reaction of zinc oxide thin films with lithium. J Electrochem Soc. https://doi.org/10.1149/1.1570410

[6] Pelliccione CJ, Ding Y, Timofeeva EV, Segre CU (2015) In Situ XAFS study of the capacity fading mechanisms in ZnO anodes for lithium-ion batteries. J Electrochem Soc. https://doi.org/10.1149/2.1011509jes

[7] Mueller F, Geiger D, Kaiser U, Passerini S, Bresser D (2016) Elucidating the impact of cobalt doping on the lithium storage mechanism in conversion/alloying-type zinc oxide anodes. ChemElectroChem. https://doi.org/10.1002/celc.201600179

[8] Hao Y, Wang S, Zeng J, Li H, Yang P, Liu B, Zhang S, Xing Y (2018) A peapod-like ZnO@C design with internal void space to relieve its large-volume-change as lithium-ion battery anode. Ceram Int. https://doi.org/10.1016/j.ceramint.2017.08.088

[9] Park M-G, Sung G-K, Sung N-E, Kim J-H, Park C-M (2016) Partially reversible Li2O formation in ZnO: a critical finding

[10] Jamnik J, Maier J (2003) Nanocrystallinity effects in lithium battery materials. Phys Chem. https://doi.org/10.1039/b309130a

[11] Xiao L, Li E, Yi J, Meng W, Wang S, Deng B, Liu J (2018) Enhancing the performance of nanostructured ZnO as an anode material for lithium-ion batteries by polydopamine-derived carbon coating and confined crystallization. J Alloy Compd. https://doi.org/10.1016/j.jallcom.2018.06.081

[12] Abbas SM, Hussain ST, Ali S, Ahmad N, Ali N, Abbas S (2013) Structure and electrochemical performance of ZnO/CNT composite as anode material for lithium-ion batteries. J Mater Sci. https://doi.org/10.1007/s10853-013-7336-3

[13] Hsieh C-T, Lin C-Y, Chen Y-F, Lin J-S (2013) Synthesis of ZnO@Graphene composites as anode materials for lithium ion batteries. Electrochim Acta. https://doi.org/10.1016/j.electacta.2013.07.197

[14] Quartarone E, Dall'Asta V, Resmini A, Tealdi C, Tredici IG, Tamburini UA, Mustarelli P (2016) Graphite-coated ZnO nanosheets as high-capacity, highly stable, and binder-free anodes for lithium-ion batteries. J Power Sources. https://doi.org/10.1016/j.jpowsour.2016.04.107

[15] Yang T, Liu Y, Huang Z, Liu J, Bian P, Ling CD, Liu H, Wang G, Zheng R (2018) In situ growth of ZnO nanodots on carbon hierarchical hollow spheres as high-performance electrodes for lithium-ion batteries. J Alloy Compd. https://doi.org/10.1016/j.jallcom.2017.11.125

[16] Shen L, Wang C (2015) ZnO/C microboxes derived from coordination polymer particles for superior lithium ion battery anodes. RSC Adv. https://doi.org/10.1039/C5RA18254A

[17] Bai Z, Zhang Y, Fan N, Guo C, Tang B (2014) One-step synthesis of ZnO@C nanospheres and their enhanced performance for lithium-ion batteries. Mater Lett. https://doi.org/10.1016/j.matlet.2013.12.060

[18] Zhao Q, Xie H, Ning H, Liu J, Zhang H, Wang L, Wang X, Zhu Y, Li S, Wu M (2018) Intercalating petroleum asphalt into electrospun ZnO/Carbon nanofibers as enhanced free-standing anode for lithium-ion batteries. J Alloy Compd. https://doi.org/10.1016/j.jallcom.2017.12.091

[19] Liu Y, Li Y, Zhong M, Hu Y, Hu P, Zhu M, Li W, Li Y (2016) A facile synthesis of core-shell structured ZnO@C nanosphere and their high performance for lithium ion battery anode. Mater Lett. https://doi.org/10.1016/j.matlet.2016.02.112

[20] Rangel-Mendez JR, Matos J, Cházaro-Ruiz LF, González-Castillo AC, Barrios-Yáñez G (2018) Microwave-assisted synthesis of C-doped TiO2 and ZnO hybrid nanostructured

materials as quantum-dots sensitized solar cells. Appl Surf Sci. https://doi.org/10.1016/j.apsusc.2017.10.236

[21] Xue J, Ma S, Zhou Y, Zhang Z (2015) Facile synthesis of ZnO-C nanocomposites with enhanced photocatalytic activity. Chem New J. https://doi.org/10.1039/C4NJ02004A

[22] Xiao C, Zhang S, Wang S, Xing Y, Lin R, Wei X, Wang W (2016) ZnO nanoparticles encapsulated in a 3D hierarchical carbon framework as anode for lithium ion battery. Electrochim Acta. https://doi.org/10.1016/j.electacta.2015.11.045

[23] Liu H, Shi L, Li D, Yu J, Zhang H-M, Ullah S, Yang B, Li C, Zhu C, Xu J (2018) Rational design of hierarchical ZnO@Carbon nanoflower for high performance lithium ion battery anodes. J Power Sources. https://doi.org/10.1016/j.jpowsour.2018.03.047

[24] Xie Q, Zhang X, Wu X, Wu H, Liu X, Yue G, Yang Y, Peng D-L (2014) Yolk-shell ZnO-C microspheres with enhanced electrochemical performance as anode material for lithium ion batteries. Electrochim Acta. https://doi.org/10.1016/j.electacta.2014.02.003

[25] Wei D, Xu Z, Wang J, Sun Y, Zeng S, Li W, Li X (2017) A one-pot thermal decomposition of C 4 H 4 ZnO 6 to ZnO@carbon composite for lithium storage. J Alloy Compd. https://doi.org/10.1016/j.jallcom.2017.04.214

[26] Zakharova GS, Ottmann A, Möller L, Andreikov EI, Fattakhova ZA, Puzyrev IS, Zhu Q, Thauer E, Klingeler R (2018) TiO2/C nanocomposites prepared by thermal annealing of titanium glycerolate as anode materials for lithium-ion batteries. J Mater Sci. https://doi.org/10.1007/s10853-018-2488-9

[27] Dong H, Feldmann C (2012) Porous ZnO platelets via controlled thermal decomposition of zinc glycerolate. J Alloy Compd. https://doi.org/10.1016/j.jallcom.2011.10.004

[28] Zubavichus Y, Shaporenko A, Grunze M, Zharnikov M (2005) Innershell absorption spectroscopy of amino acids at all relevant absorption edges. J Phys Chem. https://doi.org/10.1021/jp0535846

[29] Wang Y, Alsmeyer DC, McCreery RL (1990) Raman spectroscopy of carbon materials: structural basis of observed spectra. Mater Chem. https://doi.org/10.1021/cm00011a018

[30] Kumar R, Singh RK, Kumar Dubey P, Singh DP, Yadav RM, Tiwari RS (2015) Hydrothermal synthesis of a uniformly dispersed hybrid graphene–TiO2 nanostructure for optical and enhanced electrochemical applications. RSC Adv. https://doi.org/10.1039/C4RA06852A

[31] Akhavan O, Abdolahad M, Esfandiar A, Mohatashamifar M (2010) Photodegradation of graphene oxide sheets by TiO2 nanoparticles after a photocatalytic reduction. J Phys Chem C. https://doi.org/10.1021/jp103472c

[32] Ferrari AC, Robertson J (2000) Interpretation of Raman spectra of disordered and amorphous carbon. Rev B Phys. https://doi.org/10.1103/PhysRevB.61.14095

[33] Cho NH, Veirs DK, Ager JW, Rubin MD, Hopper CB, Bogy DB (1992) Effects of substrate temperature on chemical structure of amorphous carbon films. J Appl Phys. https://doi.org/10.1063/1.351122

[34] Deldicque D, Rouzaud J-N, Velde B (2016) A Raman–HRTEM study of the carbonization of wood: a new Raman-based paleothermometer dedicated to archaeometry. Carbon. https://doi.org/10.1016/j.carbon.2016.02.042

[35] Yan Y, Wang B, Yan C, Kang DJ (2019) Decorating ZnO nanoflakes on carbon cloth: free-standing, highly stable lithium-ion battery anodes. Ceram Int. https://doi.org/10.1016/j.ceramint.2019.05.097

[36] Chen X, Wang X, De Fang K (2020) A review on C1s XPS-spectra for some kinds of carbon materials. Fullerenes Nanotubes Carbon Nanostruct. https://doi.org/10.1080/1536383X.2020.1794851

[37] Rouquerol J, Avnir D, Fairbridge CW, Everett DH, Haynes JM, Pernicone N, Ramsay JDF, Sing KSW, Unger KK (1994) Recommendations for the characterization of porous solids (Technical Report). Pure Appl Chem. https://doi.org/10.1351/pac199466081739

[38] Ottmann A, Scholz M, Haft M, Thauer E, Schneider P, Gellesch M, Nowka C, Wurmehl S, Hampel S, Klingeler R (2017) Electrochemical magnetization switching and energy storage in manganese oxide filled carbon nanotubes. Sci Rep. https://doi.org/10.1038/s41598-017-14014-7

[39] Fujieda T, Takahashi S, Higuchi S (1992) Cycling behaviour of electrodeposited zinc alloy electrode for secondary lithium batteries. J Power Sources. https://doi.org/10.1016/0378-7753(92)80016-5

[40] Wang J, King P, Huggins R (1986) Investigations of binary lithium-zinc, lithium-cadmium and lithium-lead alloys as negative electrodes in organic solvent-based electrolyte. Solid State Ionics. https://doi.org/10.1016/0167-2738(86)90212-2

[41] Zhang CQ, Tu JP, Yuan YF, Huang XH, Chen XT, Mao F (2007) Electrochemical performances of Ni-coated ZnO as an anode material for lithium-ion batteries. J Electrochem Soc. https://doi.org/10.1149/1.2400609

[42] Xiao L, Mei D, Cao M, Qu D, Deng B (2015) Effects of structural patterns and degree of crystallinity on the performance of nanostructured ZnO as anode material for lithium-ion batteries. J Alloy Compd. https://doi.org/10.1016/j.jallcom.2014.11.195

[43] Winter M (1998) Graphites for lithium-ion cells: the correlation of the first-cycle charge loss with the Brunauer-

Emmett-Teller surface area. J Electrochem Soc. https://doi.org/10.1149/1.1838281

[44] Pender JP, Jha G, Youn DH, Ziegler JM, Andoni I, Choi EJ, Heller A, Dunn BS, Weiss PS, Penner RM, Mullins CB (2020) Electrode degradation in lithium-ion batteries. ACS Nano. https://doi.org/10.1021/acsnano.9b04365

[45] Poizot P, Laruelle S, Grugeon S, Dupont L, Tarascon JM (2000) Nano-sized transition-metal oxides as negative-electrode materials for lithium-ion batteries. Nature. https://doi.org/10.1038/35035045

[46] Guo Y-G, Hu J-S, Wan L-J (2008) Nanostructured materials for electrochemical energy conversion and storage devices. Mater Adv. https://doi.org/10.1002/adma.200800627

[47] Li H, Zhou H (2012) Enhancing the performances of Li-ion batteries by carbon-coating: present and future. Chem Commun 2:10. https://doi.org/10.1039/c1cc14764a

[48] Ge Y, Jiang H, Zhu J, Lu Y, Chen C, Hu Y, Qiu Y, Zhang X (2015) High cyclability of carbon-coated TiO_2 nanoparticles as anode for sodium-ion batteries. Electrochim Acta. https://doi.org/10.1016/j.electacta.2015.01.086

[49] Zhang W-M, Wu X-L, Hu J-S, Guo Y-G, Wan L-J (2008) Carbon coated Fe3O4 nanospindles as a superior anode material for lithium-ion batteries. Funct Mater Adv. https://doi.org/10.1002/adfm.200801386

[50] Song Y, Chen Y, Wu J, Fu Y, Zhou R, Chen S, Wang L (2017) Hollow metal organic frameworks-derived porous ZnO/C nanocages as anode materials for lithium-ion batteries. J Alloy Compd. https://doi.org/10.1016/j.jallcom.2016.10.110

[51] Fu Y, Zhong B, Chen Y, Song Y, Zhou R, Song Y, Chen S (2017) Porous ZnO@C core–shell nanocomposites as high performance electrode materials for rechargeable lithium-ion batteries. J Porous Mater. https://doi.org/10.1007/s10934-016-0297-6

[52] Yu M, Shao D, Lu F, Sun X, Sun H, Hu T, Wang G, Sawyer S, Qiu H, Lian J (2013) ZnO/graphene nanocomposite fabricated by high energy ball milling with greatly enhanced lithium storage capability. Electrochem Commun. https://doi.org/10.1016/j.elecom.2013.07.013

[53] Ren Z, Wang Z, Chen C, Wang J, Fu X, Fan C, Qian G (2014) Preparation of carbon-encapsulated ZnO tetrahedron as an anode material for ultralong cycle life performance lithium-ion batteries. Electrochim Acta. https://doi.org/10.1016/j.electacta.2014.09.038

[54] Li P, Liu Y, Liu J, Li Z, Wu G, Wu M (2015) Facile synthesis of ZnO/mesoporous carbon nanocomposites as high-performance anode for lithium-ion battery. Chem Eng J. https://doi.org/10.1016/j.cej.2015.02.077

[55] Fan H, Yu H, Zhang Y, Guo J, Wang Z, Wang H, Hao X, Zhao N, Geng H, Dai Z, Yan Q, Xu J (2017) From zinc-cyanide hybrid coordination polymers to hierarchical yolk-shell structures for high-performance and ultra-stable lithium-ion batteries. Nano Energy. https://doi.org/10.1016/j.nanoen.2017.01.043

Publisher's Note Springer Nature remains neutral with regard to jurisdictional claims in published maps and institutional affiliations.